Hanlei Wang[1], Feiyang Lou[1], Yiman Huang[1], Yang Gao[1], and Xiaotong Zhang[1]

[1]Affiliation not available

July 29, 2024

Function Extension and Implementation of MaRCoS in Low-, Mid-, and High-Field MRI Systems: A Technical Report

Hanlei Wang, Feiyang Lou, Yiman Huang, Yang Gao, and Xiaotong Zhang, *Senior Member, IEEE*

***Abstract*—The fast advancement of low-field MRI (magnetic resonance imaging) has generated a high demand for cost-effective and versatile consoles for MRI scanners. MaRCoS (MAgnetic Resonance COntrol System) is such an open-source system that has been well-tested on various low-field systems. However, due to limitations of the basic hardware, MaRCoS is constrained in its ability to support a wide range of field strengths and RF (radio-frequency) channels. In this study, we aim to port the MaRCoS console to high-field MRI systems and increase the number of RF receive channels, enabling phased-array coils and/or active EMI (electromagnetic interference) elimination techniques. A series of implementations were conducted across 0.11-, 0.5-, and 1.5-Telsa MRI systems, in order to evaluate its compatibility and performance. Promising results indicate that the extended console not only matches but, to some extent, surpasses the performance of a commercial spectrometer, particularly in terms of flexibility and accessibility. It is hoped that this study could effectively expand the scope of open-source MRI technology, making MRI scans more accessible and affordable.**

***Keywords*—Magnetic resonance imaging, low-field MRI, MRI console, embedded system, software-defined radio.**

I. Introduction

MAGNETIC Resonance Imaging (MRI) is an interdisciplinary technology that has revolutionized various fields, ranging from clinical diagnosis [1]–[3] to neuroscience research [4]–[7]. As one of the most essential components of this advanced imaging technology, the MRI spectrometer [8] (also known as a console [9], [10]), is an electronic control system that coordinates all signal generation and acquisition, shaping the overall imaging process. Specifically, the spectrometer is responsible for interfacing with the user and the MRI scanner, executing the pulse sequences, digitalizing and demodulating the MR (magnetic resonance) signals, synthesizing the RF (radio-frequency) and gradient pulses, and handling many other critical tasks [11]. Due to these complexities, conventional MRI spectrometers often become expensive, proprietary, and inflexible [12].

With the emergence of low-field MRI, the demand for cost-effective and versatile spectrometers has increased significantly [13]. These portable MRI systems require spectrometers with a compact footprint, low cost, and scalable design. Moreover, the aforementioned limitation of commercial spectrometers could potentially hinder the advancement of MRI technology in some cutting-edge research [14], [15]. To date, collective efforts have been made to develop open-interface spectrometers, overcoming these conventional challenges encountered in research and education [16], [17]. Owing to the rapid advancement of digital integrated circuits over the past few decades, solutions based on processors [18], [19], FPGA (field-programmable gate array) [20]–[27], and SDR (software-defined radio) [28]–[30] were subsequently explored. These developments paved the way for more affordable, flexible, and scalable spectrometers.

Among these modern spectrometers, Medusa [12] was particularly well-known, but not fully open-source. Subsequently, it was replaced by OCRA (Open-source Console for Real-time Acquisition) [30], which is a completely open-source solution for both hardware [31] and software [32]. The OCRA leverages an off-the-shelf SDR platform, called Red Pitaya, to establish an economical, stable, and flexible system. It features a pulse programmer capable of altering any pulse within a single scan, presenting a distinct advantage over previous solutions. The MaRCoS (MAgnetic Resonance COntrol System) [10] project not only inherits OCRA's hardware versatility but also introduces superior software and firmware solutions. The MaRCoS Graphical Environment[1] (MaRGE) [33] is a comprehensive Python-based GUI (graphical user interface) that implements a much more friendly interface not merely for scanner operators but for pulse sequence developers [34]. The MaRCoS firmware allows dynamic pulse updates based on real-time acquisition feedback. It is also capable of generating arbitrary waveforms of unlimited length for both RF and gradient pulses. Additionally, it is designed to independently configure the frequencies of transmitted and received carriers during mid-sequence, creatively unifying the treatment of RF and gradient pulses. Empowered by its advanced features, MaRCoS has been successfully applied in both laboratory and

Manuscript received April xx, 2024; revised August xx, 2024.*(Corresponding author: Xiaotong Zhang)*

Hanlei Wang is with the Interdisciplinary Institute of Neuroscience and Technology, College of Biomedical Engineering and Instrument Science, Zhejiang University, Hangzhou 310058, China (e-mail: volatile_static@zju.edu.cn).

Feiyang Lou is with the School of Medicine, Zhejiang University, Hangzhou 310058, China (e-mail: fylou@zju.edu.cn).

Yiman Huang is with the College of Electrical Engineering, Zhejiang University, Hangzhou 310058, China (e-mail: huangyiman@zju.edu.cn)

Yang Gao is with the College of Electrical Engineering, Zhejiang University, Hangzhou 310058, Zhejiang University, Hangzhou, China (e-mail: gaoyang2016@zju.edu.cn)

Xiaotong Zhang is with the College of Electrical Engineering, MOE Frontier Science Center for Brain Science and Brain-Machine Integration, and the Second Affiliated Hospital, Zhejiang University School of Medicine, Zhejiang University, Hangzhou 310058, China (e-mail: zhangxiaotong@zju.edu.cn).

[1]It was originally named MaRGA (MaRCoS Graphical Application).

clinical environments [35], [36].

However, MaRCoS currently lacks sufficient Rx (receiver) channels for active EMI (electromagnetic interference) elimination techniques [37]–[39], which are critical for portable MRI scanners. Moreover, phased-array coils have been widely used in high-field systems and are anticipated to be applied in low-field systems [40]. To address these limitations, this study aims to increase its Rx channels by upgrading its SDR components, and meanwhile extend the compatibility of the MaRCoS console to high-field MRI systems. The electrical characteristics of the upgraded MaRCoS console were evaluated, and saline phantom images were acquired under various magnetic fields or pulse sequences. By comparing the upgraded console with both of its predecessor and commercial alternatives[2], this study demonstrates the console's enhanced performance and robustness, highlighting its potential for broader applications in MRI research and clinical practice.

II. Materials and Methods

A. Introducing the Open-Source Solution

Here, we introduce the state-of-the-art solution and highlight the advanced features of MaRCoS, including those inherited or different from OCRA. Next, we demonstrate the process of prototyping a MaRCoS console from the ground up, thus revealing its adaptability and robustness, which are fundamental to the ongoing development efforts.

1) System Architecture: Fig. 1 illustrates the physical connection between MaRCoS console and other components of an MRI scanner, which is quite similar to OCRA. A spectrometer involves hardware/software co-design [41]. Viewed from a hierarchical perspective, the architecture can be divided into three layers, as illustrated in Fig. 3. From the perspective of modularity, however, the system consists of RF links, gradient generators, a sequence programmer, and a user interface.

2) The RF Links: Fig. 3 illustrates how the RF data is constructed from sequence parameters, compiled as machine code, modulated by the DDS (direct digital synthesis), converted to analog signals, amplified by PA, exciting MR signal in coil, boosted by LNA, demodulated in PL, reordered to k-Space, reconstructed to image, and finally saved or displayed to PC (personal computer). The start point and end point of the entire link are located in the top layer—Software. The physical bridge between the transmitting and receiving links is an RF coil located in the bottom layer—Hardware. The most critical part of the RF link is the demodulator, which greatly affects the SNR (signal-to-noise ratio) of the received signal. In MaRCoS, the demodulator is located in the middle layer—Firmware.

3) Gradient Waveform Generator: The gradient pulses are generated by the console to encode spatial information for imaging. The resolution of that generator finally determines the resolution of the image. In MaRCoS, SPI controller modules are implemented in PL of Zynq to transfer the gradient waveform to OCRA1 board, as shown in Fig. 2.

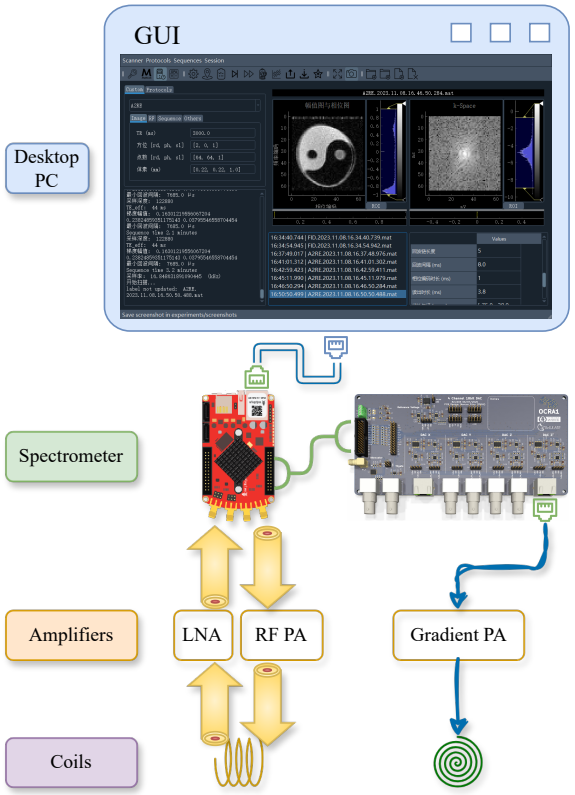

Fig. 1. The hardware connection between the MaRCoS console and the MRI scanner comprises four layers, with Desktop, Spectrometer, Amplifiers, and Coils from top to bottom. Red Pitaya (rp-122) is connected to a PA (power amplifier) via Ethernet (RJ-45). The RF signals are transmitted through a coaxial cable. The RF output and input of Red Pitaya are amplified by a PA and LNA (low-noise amplifier), respectively. In the spectrometer, gradient waveforms are converted to analog differential pairs with the RJ-45 connector by OCRA1 board. It is then amplified by gradient amplifiers and sent to linear gradient coils.

4) Pulse Sequence Programming Platform: The pulse programmer is one of the most unique parts of MaRCoS. It is capable of dynamically updating the pulse sequence in a fine time granularity, including the RF and gradient pulses. This feature is achieved by the methodology of decoupling the logic of sequences from the firmware details. In other words, the console can be treated as an arbitrary waveform generator, despite how the pulse sequence looks. Moreover, it provides a sequence compiler that can convert Python-based sequence code to machine code, improving the efficiency of pulse sequence development. The only interface that the compiler accepts is "Array". It treats all signals[3] as "first-class entities", meaning that they have the same format and can be executed in the same way. MaRCoS borrowed the server-client pattern from OCRA. The client and server communicate with each other through a TCP/IP socket. Once the client requests an acquisition, the server executes the provided pulse sequence and then responds with the acquired data. Generally, the only task of the server is to communicate with those above and those below. Below the server, binary data of pulse sequences

[2]EVO Spectrometer from MR SOLUTIONS (https://www.mrsolutions.com/).

[3]Such as RF pulses, gradient waveforms, ADC (analog-to-digital converter) triggers, and even GPIOs (general-purpose input/outputs).

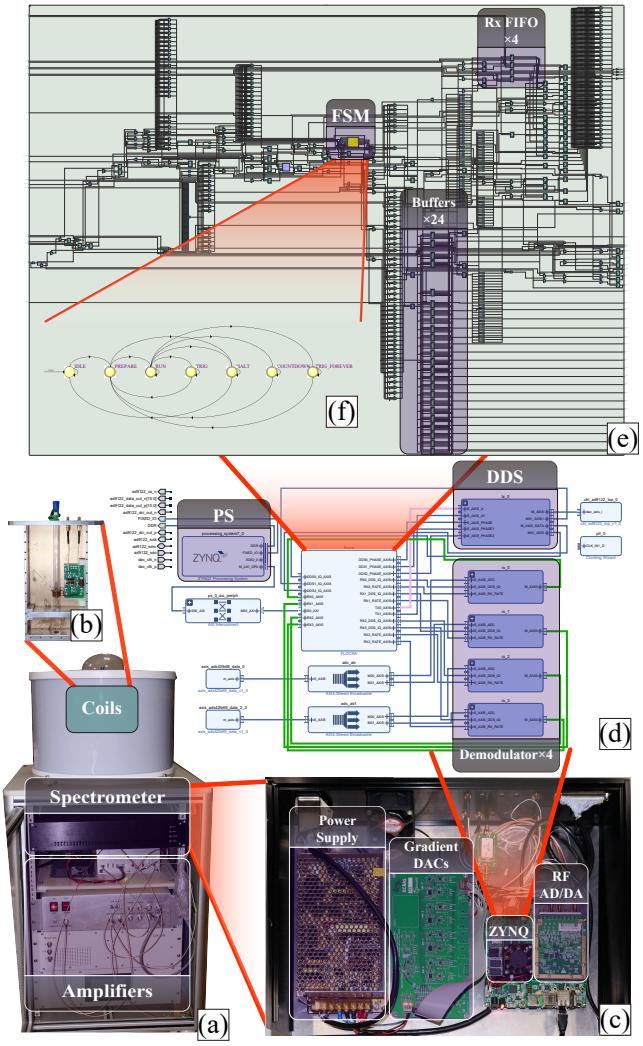

Fig. 2. Exploded view of a tabletop MRI system with extended MaRCoS hardware. (a) Tabletop MRI scanner. Inside the permanent magnet, there are RF and gradient coils. Below the magnet, there are a spectrometer, RF amplifier, and gradient amplifiers. (b) A solenoid RF coil and 1 cm diameter tube within the electromagnetic shielding copper. (c) The extended MaRCoS spectrometer. An OCRA1 board (Gradient DACs) is connected to the QT7020 board (Zynq and RF ADC/DAC) via SPI (serial peripheral interface). (d) Block design of the Zynq firmware, generated by Vivado. Complex signals for RF transmit and receive are highlighted in pink and green, respectively. The Rx (receiver) demodulators are extended to four channels. (e) RTL (register-transfer level) schematic of the pulse programmer core, generated by Quartus. Rx FIFOs (first-in-first-outs) and Buffers are extended. (f) FSM (finite state machine) to control the PL (programmable logic) and communicate with the PS (processing system) in Zynq.

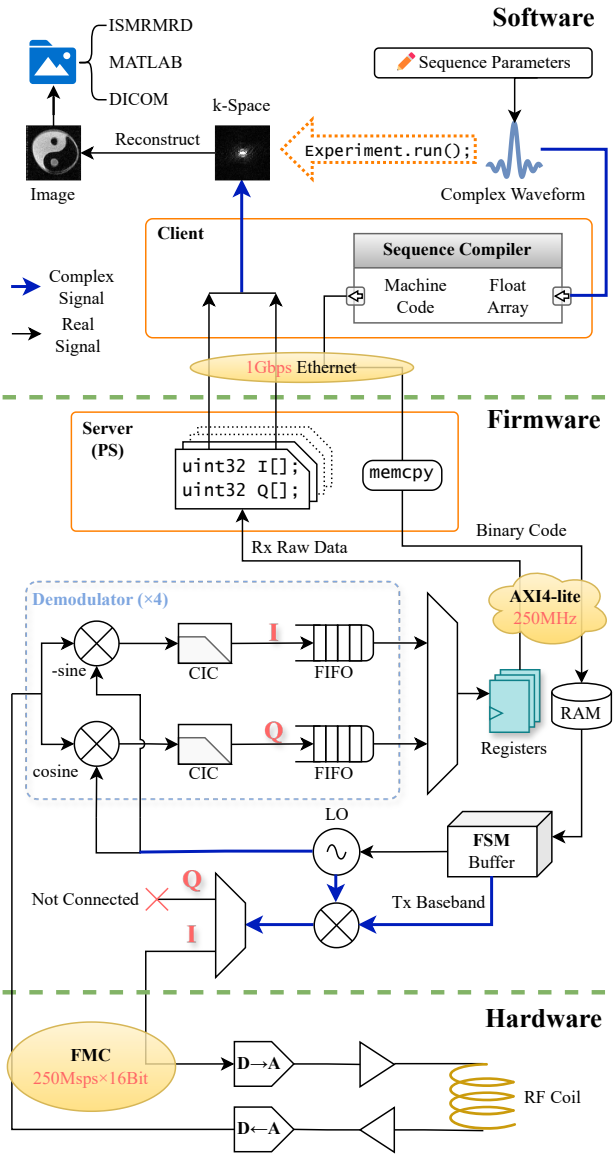

Fig. 3. The RF link of the MaRCoS console passes through three layers from top to bottom: software, firmware, and hardware. Blue arrows indicate complex data flow and black arrows indicate real data flow. Bus speed of FMC (FPGA mezzanine card) connector and AXI4-lite are extended to 250 MHz. The Rx demodulators are extended to four channels. The digitalized signal is decomposed into I/Q components through quadrature demodulation. Here the modulator and demodulators share the same LO (local oscillator), meaning that the carrier of the transmitted signal is the same as the received signal.

are stored in on-chip block RAM (random-access memory) and then executed by the FSM, shown in Fig. 2(e). Above the client, a Python class named "Experiment" is exposed to GUI. As indicated by the dotted arrow in Fig. 3, all processes of an "experiment" are encapsulated in one-key "run".

5) Graphical User Interface (GUI): MaRGE provides a comprehensive infrastructure for pulse sequence development and data post-processing. There are some useful calibration sequences (screenshots in Fig. 4), such as first-order shimming, T_1 and T_2 measurement, etc.

B. Migrating the Hardware

To begin with, we substituted the Red Pitaya board with another off-the-shelf SDR platform, QT7020 from Queentest Technology. Similar to Red Pitaya, the core of QT7020 is a Xilinx Zynq-7020 SoC (system-on-chip) with dual-core Cortex-A9 processors. However, the QT7020 has more logic resources, enabling larger sampling depth and more digital receivers. The ADC clock rate of QT7020 is configured to 250 MHz, and the on-chip PLL (phase-locked loop) of Zynq is modified to generate a 250 MHz clock domain, which is approximately twice the 122.88 MHz of Red Pitaya. In accordance with the Nyquist theorem, a 250 MHz sampling

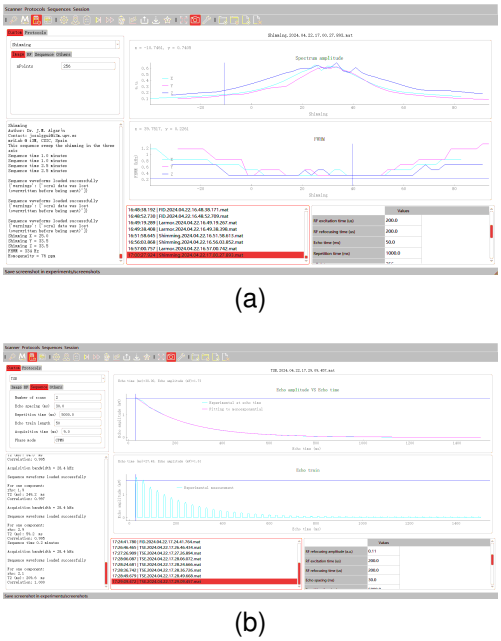

Fig. 4. Screenshots of the MaRGE. (a) First-order shimming sequence. (b) T_2 measurement sequence.

rate enables the console to handle a B_0 field strength of nearly 3-Telsa. In addition, QT7020 has a higher ADC resolution than Red Pitaya (16 bit versus 14 bit), thus we insert a stream converter in PL.

Regarding the gradient, the OCRA1 board was chosen to drive gradient amplifiers which are shown in Fig 2(a). Additionally, the necessity for loading firmware from PC to Red Pitaya at each startup has been eliminated. This is achieved by solidifying the PL firmware into an on-board flash. In this part, the PS server does not need to be modified but can be launched by Linux automatically. Lastly, all hardware components are assembled into a compact case, as shown in Fig. 2(c).

C. Inscreasing RF Channels

The original MaRCoS console supports two RF receive channels. To increase the number of receivers, we upgraded the console from software to hardware. Meanwhile, we tried to keep the backward compatibility of the original console.

1) Buffer and FIFO: Fig. 2(e) and Fig. 3 depict the extended Buffers and Rx FIFOs. The Buffers are used to store the sequence commands to be executed. The original solution utilizes one Buffer each Rx for decimation rate, and two Rx share another Buffer for commands like reset, valid, or enable. To add two more Rx, we doubled the number of Buffers. Consequently, the extended console has two Buffers for commands and four Buffers for decimation rate. The Rx FIFO is used to store the received baseband signals, which are output from the CIC (cascaded integrator-comb) filter in the demodulator and read by the server in PS. Two FIFO modules were added to increase the number of receivers.

2) Toplevel Block Design: Fig. 2(d) and Fig. 3 (dashed box) depict the extended demodulators. With above approaches, the extended RTL firmware is compatible with the original Server and Client.

3) Server: Server polls Rx FIFOs via AXI4-lite bus, and then sends the raw data to Client. An extra function is defined here to access the newly added Rx FIFOs. So far, the server is compatible with the original Client as well.

4) Client: Sequence compiler was also extended to support the new Buffers and receive more data from new FIFOs. The upgraded Client code is still compatible with the original MaRGE.

5) Pulse Sequence: Python-based pulse sequence code can be effortlessly extended to support more receivers. A special MSE (multi-spin-echo) sequence was designed to test 4-channel parallel imaging and to show the rapid development on MaRCoS platform. Fig. 5 is a diagram of the proposed 3D MSE sequence in a TR (repetition time). A major difference from simple 3D MSE is that images from every echo are averaged together to improve the SNR. In addition, an extra sampling window was inserted before the excitation pulse to acquire EMI noise for active denoising. After all shots, two matrixes of 3D k-Space with the same size were obtained, one for noise and the other for signal.

D. MRI Experiment Setup

All pulse sequence parameters are included in Table I, and other important details are introduced as follows:

1) Scanners: Characteristics of three MRI systems used in this study are listed in Table II. First, a bedside scanner using a 0.11T yoke magnet is placed in an industrial environment under no EMI screening condition. A piece of copper cloth can be covered on the magnet for electromagnetic shielding as needed. It is equipped with a knee coil, a wrist coil, and various EMI sensing coils [Fig. 6(a)]. Second, a tabletop scanner used a 0.5T yoke Sm-Co magnet with implanted temperature control to avoid field drift, shown in Fig. 2(a). Samples can be placed in an NMR (nuclear magnetic resonance) tube with a solenoid RF coil, encapsulated by a copper plate box to achieve EMI screening, as shown in Fig. 2(b). Third, a 1.5T superconducting system with "0" helium volatile is installed in an RF-shielded room. It is equipped with a high-pass birdcage coil with a 20 cm diameter and 8 rungs, shown in Fig. 6(b). Its gradient amplifiers employ closed-loop current control with adjustable gain.

2) Samples: Phantoms and fruits were used in the experiments, as the third column of Table I shows. Phantom A and Phantom B are 1-cm diameter NMR tubes filled with saline solution, while Phantom A has a 3D-printed hollow cylinder inserted. Phantom C is a cylinder measuring 13 cm in height and 10 cm in internal diameter, filled with saline solution, and this phantom was used to compare across 0.11T and 1.5T scanners.

3) Sequences: As noted in Table I, either GRE (gradient-recalled echo) or MSE sequences were used in all experiments. The MSE sequence is described in Section II-C5. When using MSE sequence, the ESP (echo spacing) represents the period between the center of adjacent echoes, and the ETL represents the number of echoes (also averages) in one phase encode

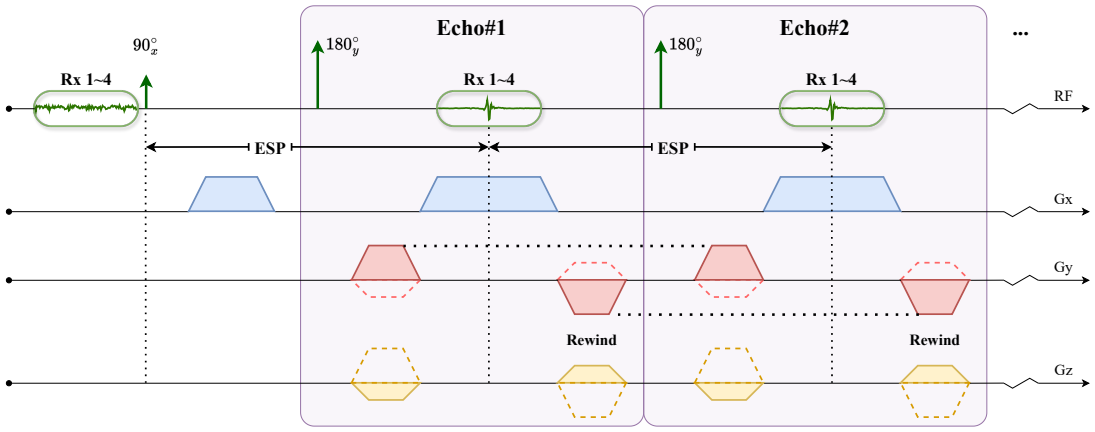

Fig. 5. Schematic of the 3D MSE (multi-spin-echo) sequence. One shot with ETL (echo train length) = 2 is shown. Within each TR, one purple box repeats for ETL times. The first sampling window—before the RF excitation pulse—is used to acquire EMI noise, and the following windows are used to acquire MR signals. During each sampling window, all of the four receivers (Rx 1∼4) are working in parallel. For each RF refocusing pulse, the CPMG (Carr-Purcell-Meiboom-Gill) phase is employed. The phase encode pulse is replayed before and rewound after each readout pulse. As demonstrated in the Gy and Gz axes, for example, the solid trapezoid represents a phase encode step and the dashed trapezoid represents another.

TABLE I
ACQUISITION PARAMETERS OF IMAGE RESULTS

Figure	B_0 (T)	Sample	RF Coil	Sequence	Rx BW (kHz)	TE / ESP (ms)	Nex*/ ETL	TR (ms)	Number of pixels (slice, phase, readout)	Scan time (min:sec)
8(a)	0.11	Star fruit	Knee	GRE	85.9	2.3	3	160	4 × 128 × 128	1:22
8(b)	0.5	Phantom A	Solenoid	MSE	31.2	6	8	2000	1 × 64 × 64	2:08
9	0.5	Phantom B	Solenoid	GRE	87.67	0.9	6	10	1 × 64 × 64	0:04
10(a)	0.11	Bamboo shoot	Wrist	MSE	6.5	15	3	300	4 × 64 × 128	1:17
10(b)	0.11	Bamboo shoot	Wrist	GRE	42.6	10	1	200	4 × 64 × 128	0:51
10(c)	0.11	Orange	Knee	GRE	28.4	14.7	3	60	8 × 128 × 128	3:05
10(d)	0.11	Orange	Knee	MSE	6.48	30	3	200	7 × 128 × 128	3:00
10(e)	0.11	Pineapple	Knee	MSE	6.48	30	3	250	8 × 128 × 128	4:16
10(f)	0.11	Pineapple	Knee	MSE	5.8	30	3	350	10 × 100 × 200	5:50
11(a)	0.11	Phantom C	Knee	GRE	28.4	14.7	2	60	20 × 128 × 128	5:07
11(b)	0.11	Phantom C	Knee	GRE	20.0	14.7	2	60	40 × 128 × 256	10:14
11(c)	0.11	Phantom C	Knee	MSE	7.79	30	2	250	20 × 128 × 128	10:40
12(a)	1.5	Phantom C	Birdcage	GRE	46.85	4.7	2	150	16 × 128 × 128	10:14
12(b)	1.5	Phantom C	Birdcage	GRE	20.0	15	1	300	16 × 128 × 128	10:14
??	0.11	Phantom C	Knee & 2 EMI	MSE	6.48	15	2	200	16 × 128 × 128	6:50
??	0.11	Pineapple	Knee & 3 EMI	MSE	6.48	15	3	600	8 × 64 × 128	5:07

* Number of experiments (averages).

TABLE II
CHARACTERISTICS OF USED MRI SYSTEMS

B_0	0.11T	0.5T	1.5T
f_L (**MHz**)	4.4276	20.797	63.767
DSV*(**cm**)	22	1	25
Rx Gain (**dB**)	48	48	66
RF PA (**W**)	300	100	2000
Gradient PA (**A/V**)	12	1	PID**

* Diameter of spherical volume.
** Proportional-Integral-Derivative controller.

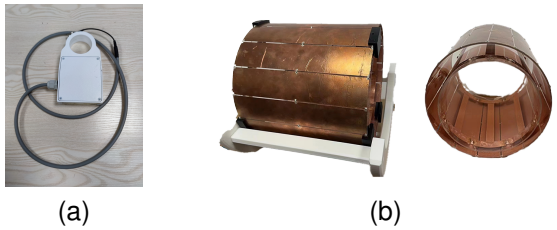

Fig. 6. Photographs of the EMI sensing coil (a) and birdcage coil (b).

step. A 3D GRE sequence provided by MaRGE was used to compare the MaRCoS console against the EVO Spectrometer (MR SOLUTIONS). When using the GRE sequence, the T_E represents echo time and the Nex represents the number of averages. Although some timing details may be different, we kept parameters as same as possible in the two consoles.

III. RESULTS AND DISCUSSION

A. Electrical Characteristics

The maximum Tx (transmitter) power of the extended MaRCoS console is -0.22 dBm. The range of gradient amplitude is near ±10 V. To evaluate the stability of the RF phase and gradient amplitude, we acquired the FID (free induction

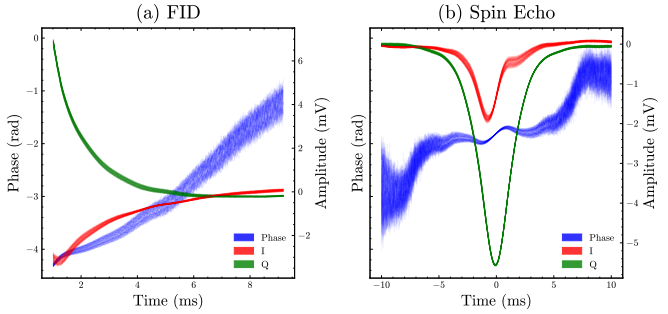

Fig. 7. The waveforms of FID (free induction decay) and SE (spin-echo) signals in 100 TR (repetition time), at 0.5T tabletop scanner. The left y-axis represents the unwrapped phase of the signal, while the right y-axis represents the amplitude of two components (I/Q) of complex signals. (a) FID sequence with TR = 2 s, Rx bandwidth = 31.3 kHz. (b) SE sequence with TR = 2 s, TE = 40 ms, Rx bandwidth = 20 kHz. The zero time point is the target center of the echo.

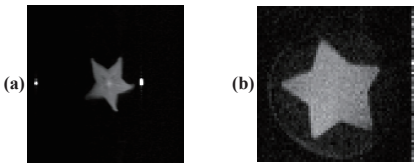

Fig. 8. Images acquired by the original MaRCoS console with the Red Pitaya board at 0.11T and 0.5T scanners. (a) A filtered image of a star fruit. The filtering approach is applying a hamming window on every readout line. (b) Image of Phantom A, a star-shaped phantom in a 1-cm diameter NMR tube.

decay) and SE (spin-echo) signals over 100 TR cycles, plotted in the same axis, as shown in Fig. 7. During each TR cycle, first-order shimming was applied 10 ms before the RF excitation pulse. The shimming gradient is typically weak but can significantly affect the amplitude and frequency of the MR signal. As a result, the stability and resolution of the gradient waveform generator, as well as the RF DAC (digital-to-analog converter) and clock jitter, can be evaluated.

B. Imaging Performance

Firstly, we acquired images by the original MaRCoS console at 0.11T and 0.5T scanners, shown in Fig. 8. There are strong artifacts in Fig. 8(a), which appeared in [34] as well. These artifacts may be caused by excessive Rx bandwidth, but were not observed in the extended 250-MHz-clock console.

Fig. 9 shows the B_0 map acquired by dual-echo GRE sequence. The TE (echo time) of the two echoes were 0.9 and 1.8 ms respectively. Distortion induced by an inhomogeneous B_0 field can be observed.

Fig. 10 showcases the imaging quality of the extended MaRCoS console. Furthermore, a comparison between the extended MaRCoS console and a commercial one (EVO Spectrometer) was taken at 0.11T (Fig. 11) and 1.5T (Fig. 12) scanners.

Due to the gradient efficiency being difficult to be well-calibrated, a precise FoV (field of view) cannot be given yet. According to the dimension of Phantom C, however, we can roughly estimate the spatial resolution to be about $1 \times 1 \times 10mm^3$, among Fig. 11, 12, and **??**.

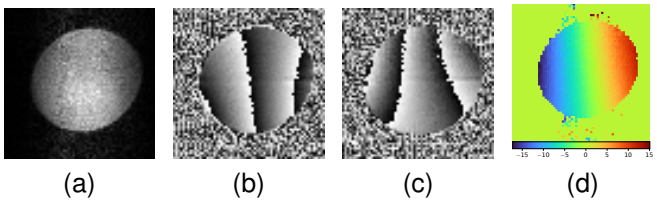

Fig. 9. (a) The image reconstructed from the first echo of a GRE sequence. (b) and (c) are the phase images of the first and second echoes, respectively. (d) The B0 map calculated from the phase images. A mask from (a) is applied to remove the background.

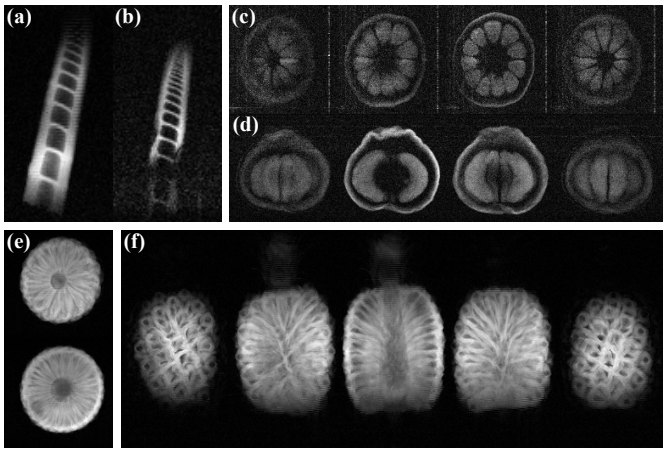

Fig. 10. Images acquired by the extended MaRCoS console at 0.11T bedside scanner with copper cloth covered. Center slices of the 3D images are shown. (a) and (b) are coronal images of a bamboo shoot, acquired by 3D MSE and GRE sequences, respectively. (c) and (d) are coronal and sagittal images of an orange, acquired by 3D GRE and MSE sequences, respectively. (e) and (f) are sagittal and coronal images of a pineapple, respectively, acquired by 3D MSE sequence.

C. Outlook

Limited by the serial processing of Server in PS, DMA (direct memory access) is required to extend a large number of receivers.

IV. Conclusion

We extended the MaRCoS console by doubling the ADC sampling rate and Rx channels. The extended console is capable of controlling MRI scanners with higher field strength up to 1.5T and handling 4-channel parallel acquisition. Active EMI elimination procedures were effectively implemented, further supporting the successful extension of the 4-channel receiver. Full source code of the extended console is available on public repository [42].

References

[1] X. Zhang, Y. Zhang, and A. W. Roe, "Ultra-high-field MRI studies of brain structure and function in humans and nonhuman primates: A collaborative approach to precision medicine," *Current Opinion in Biomedical Engineering*, vol. 20, p. 100320, Dec. 2021.

[2] M. H. Mazurek, B. A. Cahn, M. M. Yuen, A. M. Prabhat, I. R. Chavva, J. T. Shah, A. L. Crawford, E. B. Welch, J. Rothberg, L. Sacolick, M. Poole, C. Wira, C. C. Matouk, A. Ward, N. Timario, A. Leasure, R. Beekman, T. J. Peng, J. Witsch, J. P. Antonios, G. J. Falcone, K. T. Gobeske, N. Petersen, J. Schindler, L. Sansing, E. J. Gilmore, D. Y. Hwang, J. A. Kim, A. Malhotra, G. Sze, M. S. Rosen, W. T.

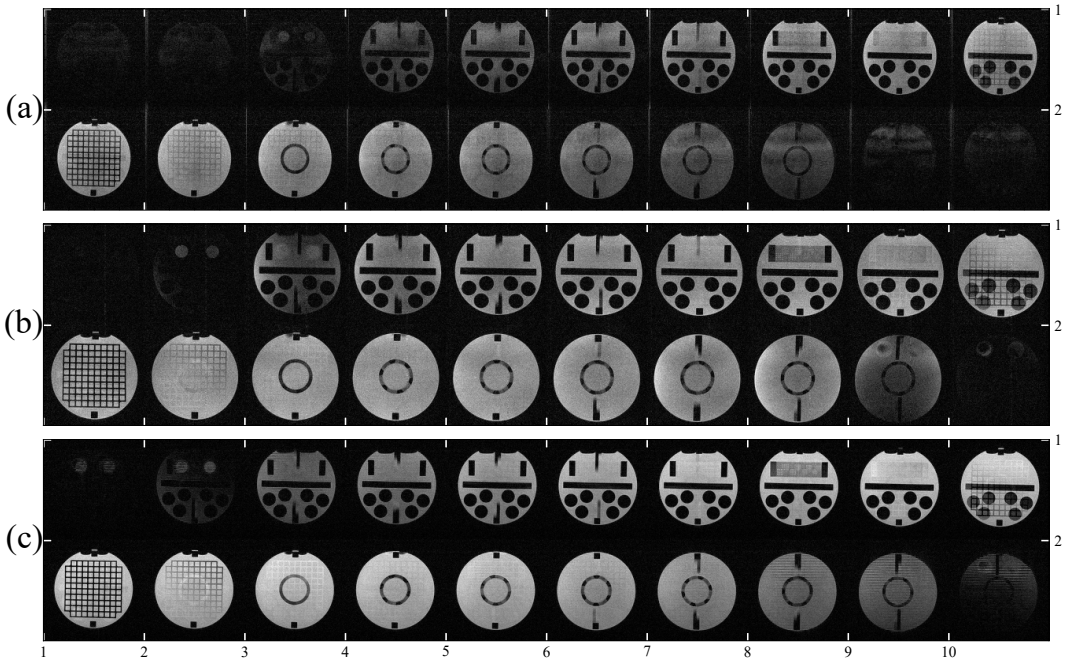

Fig. 11. The $20 \times 128 \times 128$ images of the Phantom C were acquired at 0.11T bedside scanner with a solenoid knee coil and copper cloth covered. (a) and (c) were acquired by the extended MaRCoS console, while (b) was acquired by a commercial console. To be noted, (b) has $2\times$ oversampling along G_x and G_z, yielding $2\times$ scan time compared to (a) with the same TR.

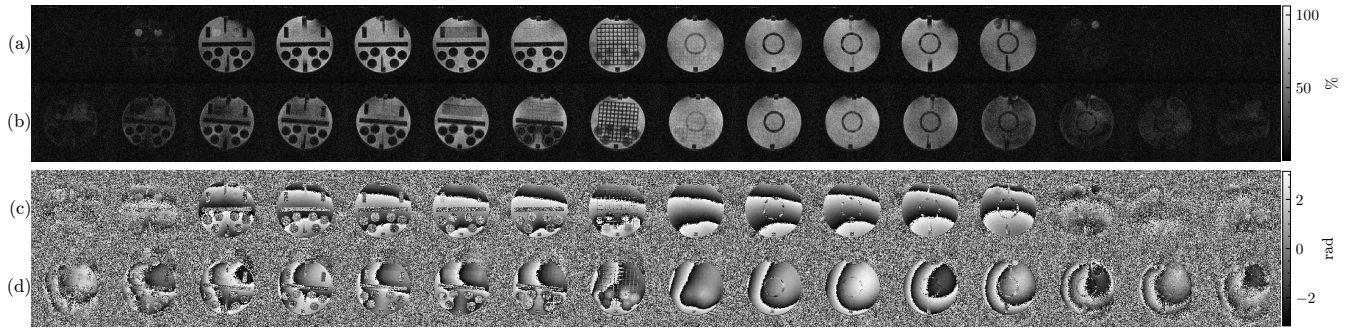

Fig. 12. Images of the Phantom C acquired by 3D GRE sequence at the 1.5T superconducting magnet with a birdcage coil. (a) Images acquired by the extended MaRCoS console. (b) Images acquired by a commercial console. (c) and (d) are the phase graphs of (a) and (b), respectively.

Kimberly, and K. N. Sheth, "Portable, bedside, low-field magnetic resonance imaging for evaluation of intracerebral hemorrhage," *Nature Communications*, vol. 12, no. 1, p. 5119, Dec. 2021.

[3] W. T. Kimberly, A. J. Sorby-Adams, A. G. Webb, E. X. Wu, R. Beekman, R. Bowry, S. J. Schiff, A. de Havenon, F. X. Shen, G. Sze, P. Schaefer, J. E. Iglesias, M. S. Rosen, and K. N. Sheth, "Brain imaging with portable low-field MRI," *Nature Reviews Bioengineering*, vol. 1, no. 9, pp. 617–630, Sep. 2023, publisher: Nature Publishing Group.

[4] N. K. Logothetis, J. Pauls, M. Augath, T. Trinath, and A. Oeltermann, "Neurophysiological investigation of the basis of the fMRI signal," *Nature*, vol. 412, no. 6843, pp. 150–157, Jul. 2001.

[5] N. K. Logothetis, "What we can do and what we cannot do with fMRI," *Nature*, vol. 453, no. 7197, pp. 869–878, Jun. 2008.

[6] J. Wang, X. Du, S. Yao, L. Li, H. Tanigawa, X. Zhang, and A. W. Roe, "Mesoscale organization of ventral and dorsal visual pathways in macaque monkey revealed by 7T fMRI," *Progress in Neurobiology*, vol. 234, p. 102584, Mar. 2024.

[7] R. J. Huster, S. Debener, T. Eichele, and C. S. Herrmann, "Methods for Simultaneous EEG-fMRI: An Introductory Review," *Journal of Neuroscience*, vol. 32, no. 18, pp. 6053–6060, May 2012.

[8] G. N. Holland, J. R. Macfall, and I. S. o. t. S. B. S. Council, "An overview of digital spectrometers for MR imaging," *Journal of Magnetic Resonance Imaging*, vol. 2, no. 2, pp. 241–246, 1992.

[9] W. Tang, W. Wang, W. Liu, Y. Ma, X. Tang, L. Xiao, and J.-H. Gao, "A home-built digital optical MRI console using high-speed serial links," *Magnetic Resonance in Medicine*, vol. 74, no. 2, pp. 578–588, 2015.

[10] V. Negnevitsky, Y. Vives-Gilabert, J. M. Algarín, L. Craven-Brightman, R. Pellicer-Guridi, T. O'Reilly, J. P. Stockmann, A. Webb, J. Alonso, and B. Menküc, "MaRCoS, an open-source electronic control system for low-field MRI," *Journal of Magnetic Resonance*, vol. 350, p. 107424, May 2023.

[11] D. W. McRobbie, E. A. Moore, M. J. Graves, and M. R. Prince, "Let's talk technical: Mr equipment," in *MRI from Picture to Proton*. Cambridge University Press, 2017, pp. 144–165.

[12] P. P. Stang, S. M. Conolly, J. M. Santos, J. M. Pauly, and G. C. Scott, "Medusa: A Scalable MR Console Using USB," *IEEE Transactions on Medical Imaging*, vol. 31, no. 2, pp. 370–379, Feb. 2012.

[13] A. Webb and J. Obungoloch, "Five steps to make MRI scanners more affordable to the world," *Nature*, vol. 615, no. 7952, pp. 391–393, Mar. 2023.

[14] W. Tang, H. Sun, and W. Wang, "A digital receiver module with direct data acquisition for magnetic resonance imaging systems," *Review of Scientific Instruments*, vol. 83, no. 10, p. 104701, Oct. 2012.

[15] N. Ruipeng, D. Yidong, Y. Guang, and L. Gengying, "A digital receiver with fast frequency- and gain-switching capabilities for MRI systems," *Magnetic Resonance Materials in Physics, Biology and Medicine*,

vol. 22, no. 6, pp. 333–342, Dec. 2009.
[16] C. Z. Cooley, J. P. Stockmann, T. Witzel, C. LaPierre, A. Mareyam, F. Jia, M. Zaitsev, Y. Wenhui, W. Zheng, P. Stang, G. Scott, E. Adalsteinsson, J. K. White, and L. L. Wald, "Design and implementation of a low-cost, tabletop MRI scanner for education and research prototyping," *Journal of Magnetic Resonance*, vol. 310, p. 106625, Jan. 2020.
[17] L. Winter, J. Periquito, C. Kolbitsch, R. Pellicer-Guridi, R. G. Nunes, M. Häuer, L. Broche, and T. O'Reilly, "Open-source magnetic resonance imaging: Improving access, science, and education through global collaboration," *NMR in Biomedicine*, vol. n/a, no. n/a, p. e5052, Nov. 2023.
[18] P. Sipilä, R. F. Schulte, G. Wachutka, and F. Wiesinger, "Digital multiband receiver for magnetic resonance," *Concepts in Magnetic Resonance Part B: Magnetic Resonance Engineering*, vol. 35B, no. 4, pp. 210–220, Oct. 2009.
[19] S. Handa, T. Domalain, and K. Kose, "Single-chip pulse programmer for magnetic resonance imaging using a 32-bit microcontroller," *Review of Scientific Instruments*, vol. 78, no. 8, p. 084705, Aug. 2007.
[20] S. Hashimoto, K. Kose, and T. Haishi, "Comparison of Analog and Digital Transceiver Systems for MR Imaging," *Magnetic Resonance in Medical Sciences*, vol. 13, no. 4, pp. 285–291, 2014.
[21] K. Raoof, A. Asfour, and J. Fournier, "A complete digital magnetic resonance imaging (MRI) system at low magnetic field (0.1 Tesla)," in *IMTC/2002. Proceedings of the 19th IEEE Instrumentation and Measurement Technology Conference (IEEE Cat. No.00CH37276)*, vol. 1, May 2002, pp. 341–345 vol.1, iSSN: 1091-5281.
[22] S. Jie, X. Qin, L. Ying, and L. Gengying, "Home-built magnetic resonance imaging system (0.3 T) with a complete digital spectrometer," *Review of Scientific Instruments*, vol. 76, no. 10, p. 105101, Oct. 2005.
[23] Z. Liu, C. Zhao, H. Zhou, and H. Feng, "A Novel Digital Magnetic Resonance Imaging Spectrometer," in *2006 International Conference of the IEEE Engineering in Medicine and Biology Society*, Aug. 2006, pp. 280–283, iSSN: 1557-170X.
[24] K. Takeda, "OPENCORE NMR: Open-source core modules for implementing an integrated FPGA-based NMR spectrometer," *Journal of Magnetic Resonance*, vol. 192, no. 2, pp. 218–229, Jun. 2008.
[25] S. Hashimoto, K. Kose, and T. Haishi, "Development of a pulse programmer for magnetic resonance imaging using a personal computer and a high-speed digital input-output board," *Review of Scientific Instruments*, vol. 83, no. 5, p. 053702, May 2012.
[26] X. Liang, S. Binghe, M. Yueping, and Z. Ruyan, "A digital magnetic resonance imaging spectrometer using digital signal processor and field programmable gate array," *Review of Scientific Instruments*, vol. 84, no. 5, p. 054702, May 2013.
[27] D. Ariando, C. Chen, M. Greer, and S. Mandal, "An autonomous, highly portable NMR spectrometer based on a low-cost System-on-Chip (SoC)," *Journal of Magnetic Resonance*, vol. 299, pp. 74–92, Feb. 2019.
[28] W. Tang and W. Wang, "A single-board NMR spectrometer based on a software defined radio architecture," *Measurement Science and Technology*, vol. 22, no. 1, p. 015902, Dec. 2010.
[29] C. J. Hasselwander, Z. Cao, and W. A. Grissom, "gr-MRI: A software package for magnetic resonance imaging using software defined radios," *Journal of Magnetic Resonance*, vol. 270, pp. 47–55, Sep. 2016.
[30] S. M. . Anand, "OCRA : a low-cost, open-source FPGA-based MRI console capable of real-time control," Thesis, Massachusetts Institute of Technology, 2018. [Online]. Available: https://dspace.mit.edu/handle/1721.1/121619
[31] OCRA - open-source console for real-time acquisition. [Online]. Available: https://zeugmatographix.org/ocra/
[32] OCRA MRI - welcome. [Online]. Available: https://openmri.github.io/ocra/
[33] MaRCoS MRI, "MaRGE," GitHub, 2024. [Online]. Available: https://github.com/marcos-mri/MaRGE
[34] J. M. Algarín, T. Guallart-Naval, J. Borreguero, F. Galve, and J. Alonso, "MaRGA: a Graphical and Application Interface for MaRCoS," Dec. 2023, arXiv:2312.08711 [physics] version: 1. [Online]. Available: http://arxiv.org/abs/2312.08711
[35] T. Guallart-Naval, J. M. Algarín, R. Pellicer-Guridi, F. Galve, Y. Vives-Gilabert, R. Bosch, E. Pallás, J. M. González, J. P. Rigla, P. Martínez, F. J. Lloris, J. Borreguero, Á. Marcos-Perucho, V. Negnevitsky, L. Martí-Bonmatí, A. Ríos, J. M. Benlloch, and J. Alonso, "Portable magnetic resonance imaging of patients indoors, outdoors and at home," *Scientific Reports*, vol. 12, no. 1, p. 13147, Jul. 2022.
[36] T. Guallart-Naval, T. O'Reilly, J. M. Algarín, R. Pellicer-Guridi, Y. Vives-Gilabert, L. Craven-Brightman, V. Negnevitsky, B. Menküc, F. Galve, J. P. Stockmann, A. Webb, and J. Alonso, "Benchmarking the performance of a low-cost magnetic resonance control system at multiple sites in the open MaRCoS community," *NMR in Biomedicine*, vol. 36, no. 1, p. e4825, 2023.
[37] Y. Zhao, Y. Ding, V. Lau, C. Man, S. Su, L. Xiao, A. T. L. Leong, and E. X. Wu, "Whole-body magnetic resonance imaging at 0.05 tesla," *Science*, vol. 384, no. 6696, p. eadm7168, 2024, publisher: American Association for the Advancement of Science.
[38] Y. Liu, A. T. L. Leong, Y. Zhao, L. Xiao, H. K. F. Mak, A. C. O. Tsang, G. K. K. Lau, G. K. K. Leung, and E. X. Wu, "A low-cost and shielding-free ultra-low-field brain MRI scanner," *Nature Communications*, vol. 12, no. 1, p. 7238, Dec. 2021.
[39] L. Yang, W. He, Y. He, J. Wu, S. Shen, and Z. Xu, "Active EMI Suppression System for a 50 mT Unshielded Portable MRI Scanner," *IEEE Transactions on Biomedical Engineering*, vol. 69, no. 11, pp. 3415–3426, Nov. 2022.
[40] S. Shen, Y. Zhang, X. Kong, L. Yang, M. S. Rosen, and Z. Xu, "An Exploration of a Phased-Array RF Coil for Very Low-Field Brain MRI," *IEEE Sensors Journal*, vol. 24, no. 3, pp. 2905–2914, Feb. 2024.
[41] B. Drozdenko, M. Zimmermann, T. Dao, K. Chowdhury, and M. Leeser, "Hardware-Software Codesign of Wireless Transceivers on Zynq Heterogeneous Systems," *IEEE Transactions on Emerging Topics in Computing*, vol. 6, no. 4, pp. 566–578, Oct. 2018.
[42] volatile static, "MaRGEx," GitHub, GPL-3.0 License. [Online]. Available: https://github.com/volatile-static/MaRGEx